

Review

Advanced Fiber Sensors Based on the Vernier Effect

Yunhao Chen ^{1,2} , Li Zhao ^{1,*} , Shuai Hao ¹ and Jianing Tang ¹

¹ School of Electrical and Information Engineering, Yunnan Minzu University, Kunming 650500, China; 17B321002@stu.hit.edu.cn (Y.C.); hsgj1998@163.com (S.H.); tjn1216@163.com (J.T.)

² National Key Laboratory of Tunable Laser Technology, Institute of Opto-Electronics, Harbin Institute of Technology, Harbin 150080, China

* Correspondence: zl_817@126.com

Abstract: For decades, optical fiber interferometers have been extensively studied and applied for their inherent advantages. With the rapid development of science and technology, fiber sensors with higher detection sensitivity are needed on many occasions. As an effective way to improve measurement sensitivity, Vernier effect fiber sensors have drawn great attention during the last decade. Similar to the Vernier caliper, the optical Vernier effect uses one interferometer as a fixed part of the Vernier scale and the other as a sliding part of the Vernier scale. This paper first illustrates the principle of the optical Vernier effect, then different configurations used to produce the Vernier effect are classified and discussed. Finally, the outlook for Vernier effect fiber sensors is presented.

Keywords: Vernier effect; fiber sensor; Vernier envelope; magnification factor



Citation: Chen, Y.; Zhao, L.; Hao, S.; Tang, J. Advanced Fiber Sensors Based on the Vernier Effect. *Sensors* **2022**, *22*, 2694. <https://doi.org/10.3390/s22072694>

Academic Editors: Flavio Esposito, Stefania Campopiano and Agostino Iadicicco

Received: 1 March 2022

Accepted: 29 March 2022

Published: 31 March 2022

Publisher's Note: MDPI stays neutral with regard to jurisdictional claims in published maps and institutional affiliations.



Copyright: © 2022 by the authors. Licensee MDPI, Basel, Switzerland. This article is an open access article distributed under the terms and conditions of the Creative Commons Attribution (CC BY) license (<https://creativecommons.org/licenses/by/4.0/>).

1. Introduction

Over the past few decades, optical fiber sensors have been widely researched due to their unique merits such as compact size, remote monitoring ability, high flexibility, low propagating loss, low fabrication cost, and immunity to electromagnetic interference [1]. Large varieties of optical fiber sensors have been developed for sensing. The most commonly used interferometric optical fiber sensors include Fabry–Perot interferometers (FPI) [2], Mach–Zehnder interferometers (MZI) [3], Sagnac interferometers (SI) [4], Michelson interferometers (MI) [5], which have been extensively investigated to measure various parameters, such as temperature, strain, curvature, pressure, humidity, gas concentration, refractive index (RI), and so on. With the rapid development of science and technology, many fields put forward higher requirements for precise measurement, such as seismic wave detection, chemical concentration detection, microdeformation detection, etc. However, traditional interferometric fiber sensors still have great applications in the fields that require high detection resolution.

Leveraging on the slight scale difference between the Vernier and the main ruler, the Vernier effect was initially employed in the Vernier caliper to improve the length measurement accuracy. Recently, the Vernier effect has been revealed to be a useful technique to enhance the sensing performance of optical fiber sensors, which can greatly improve the detection resolution of fiber sensors [6,7]. In fact, the Vernier-effect-based optical fiber sensors have demonstrated a huge potential to achieve high sensitivity and resolution, and research on optical fiber sensors based on the Vernier effect rapidly became a popular topic among researchers during the last five years.

In this paper, the latest research on optical fiber sensors using the Vernier effect to improve measurement sensitivity and resolution is reviewed. First, the operating principle of the optical Vernier effect employed in the fiber interferometers is analyzed. Then, different fiber interferometer configurations used to produce Vernier effect are categorized according to the sensor type and the combination method of sensors. The comparison tables listing the achieved sensitivities, measurement ranges and magnification factors of

different configurations are presented. In the following, a special technique to produce a higher-order optical Vernier effect is discussed and analyzed, that is, the harmonic Vernier effect. Finally, this paper concludes with a short summary and outlook of the Vernier-effect-based fiber sensors.

2. Optical Vernier Effect

The Vernier effect was originally employed by the Vernier caliper to enhance the length measurement accuracy. The Vernier caliper typically utilizes a fixed scale and a sliding scale with slightly different periods. Optically, researchers recently found that the Vernier effect employed in fiber-sensing fields could magnify the sensing sensitivity. Similar to the Vernier caliper, optical fiber sensors based on the Vernier effect consist of two interferometers. One serves as the sensing part, corresponding to the sliding scale, and the other acts as the reference part and corresponds to the fixed scale. To produce the Vernier effect in a fiber sensor, two interferometers must have approximate but unequal interferometric periods. That is, they must have slightly detuned free spectral ranges (FSRs). The FSR is the wavelength interval between two adjacent interference dips. It can be modified by adjusting the optical path difference (OPD), which can be realized by changing the refractive index and/or the physical length of the fiber interferometer. The output spectrum of the fiber sensor is a superposition of the interferometric signals. It has a series of fine fringes with Vernier envelope modulation. The Vernier envelope dip/peak occurs at the position where the interferometric spectra just overlap or are closest to each other. Once the sensing spectrum shifts, the Vernier envelope presents a magnified spectral shift. By tracing the wavelength response of the extracted Vernier envelope dip/peak, the sensitivity can be amplified by orders of magnitude. The enhanced sensitivity realized by the Vernier effect is based on the tracing of the wavelength, so fiber sensors in this review all operate in the wavelength domain.

To fully clarify the operating principle of the Vernier-effect-based fiber sensors, we take a parallel structured fiber sensor as an example. The diagram of this sensor is shown in Figure 1. A 3 dB coupler is adopted to connect two fiber interferometers (FIs), and light splitting and combing are realized through the 3 dB coupler. Here it is important to point out that although the following optical Vernier effect theory is based on two reflective fiber interferometers, it can easily be extended to other types of Vernier effect fiber sensors with different configurations, such as MZI, MI, SI, or some fiber resonators.

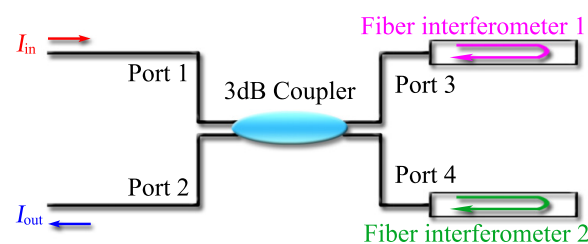


Figure 1. Vernier effect fiber sensor with two parallel connected FIs.

Considering the case in Figure 1, where two FIs are connected in parallel with a 3 dB coupler, the light emitted by the light source enters the 3 dB coupler from Port 1. In the 3 dB coupler, light is divided into two beams with the same power, then fed into two interferometers from Port 3 and Port 4, respectively. Light in the interferometer propagates along different optical path lengths, accumulating OPD, thus leading to interference. The interference signal generated in the interferometer will be reflected back, superimposed in the coupler, and finally detected through Port 2.

Assuming that the intensity of incident light is I_{in} , the corresponding electric field amplitude is E_{in} . In the fiber interferometer, light is split into two beams. With this, it can be obtained that the electric field amplitudes of the interferometric light output from interferometer 1 and interferometer 2 are as follows, respectively.

$$E_{\text{port3}}(\lambda) = A_1 \frac{E_{\text{in}}}{\sqrt{2}} + B_1 \frac{E_{\text{in}}}{\sqrt{2}} \exp \left[-i \frac{2\pi(n_{1a}L_{1a} - n_{1b}L_{1b})}{\lambda} \right] \quad (1)$$

$$E_{\text{port4}}(\lambda) = A_2 \frac{E_{\text{in}}}{\sqrt{2}} + B_2 \frac{E_{\text{in}}}{\sqrt{2}} \exp \left[-i \frac{2\pi(n_{2a}L_{2a} - n_{2b}L_{2b})}{\lambda} \right] \quad (2)$$

where λ is the wavelength of incident light, A_1 and B_1 are the amplitude reflection coefficients of two beams in interferometer 1, n_{1a} and n_{1b} are refractive indices of different fiber parts through which light travels, and L_{1a} and L_{1b} are the propagation path lengths of the two beams in interferometer 1. Similarly, A_2 , B_2 , n_{2a} , n_{2b} , L_{2a} and L_{2b} are the corresponding parameters of interferometer 2. In Equations (1) and (2), the initial transmission phase of light in two interferometers is ignored. Taking interferometer 1, for example, the relationship between m th interference dip wavelength and phase is:

$$\frac{2\pi(n_{1a}L_{1a} - n_{1b}L_{1b})}{\lambda_{\text{dip1}}(m)} = (2m + 1)\pi \quad (3)$$

The dip wavelength could be expressed as:

$$\lambda_{\text{dip1}}(m) = \frac{2\pi(n_{1a}L_{1a} - n_{1b}L_{1b})}{2m + 1} \quad (4)$$

where m is the order of the interference dip, and m is an integer.

From Equation (3), the FSRs of the two interferometers, namely, FSR_1 and FSR_2 , are obtained:

$$FSR_1 = \lambda_{\text{dip1}}(m - 1) - \lambda_{\text{dip1}}(m) = \frac{\lambda^2}{n_{1a}L_{1a} - n_{1b}L_{1b}} \quad (5)$$

$$FSR_2 = \lambda_{\text{dip2}}(m - 1) - \lambda_{\text{dip2}}(m) = \frac{\lambda^2}{n_{2a}L_{2a} - n_{2b}L_{2b}} \quad (6)$$

To facilitate the analysis, the two interferometers are assumed to be with same amplitude reflectivity, that is $A = A_1 = A_2$, $B = B_1 = B_2$, and transmission loss is ignored. Then, the electric amplitude of light output from Port 2 is:

$$\begin{aligned} E_{\text{out}}(\lambda) &= E_{\text{port3}}(\lambda) + E_{\text{port4}}(\lambda) \\ &= \sqrt{2}AE_{\text{in}} + B \frac{E_{\text{in}}}{\sqrt{2}} \left\{ \exp \left[-i \frac{2\pi(n_{1a}L_{1a} - n_{1b}L_{1b})}{\lambda} \right] + \exp \left[-i \frac{2\pi(n_{2a}L_{2a} - n_{2b}L_{2b})}{\lambda} \right] \right\} \end{aligned} \quad (7)$$

From Equation (7), the output light intensity is [8]:

$$\begin{aligned} I_{\text{port2}} &= \left| \frac{E_{\text{out}}(\lambda)}{E_{\text{in}}(\lambda)} \right|^2 = \frac{E_{\text{out}}(\lambda)E_{\text{out}}^*(\lambda)}{E_{\text{in}}^2(\lambda)} \\ &= I_0 - 2AB \{ \cos[2\pi(n_{1a}L_{1a} - n_{1b}L_{1b})/\lambda] + \cos[2\pi(n_{2a}L_{2a} - n_{2b}L_{2b})/\lambda] \} \\ &\quad + B^2 \{ 2\pi[(n_{1a}L_{1a} - n_{1b}L_{1b}) - (n_{2a}L_{2a} - n_{2b}L_{2b})]/\lambda \} \end{aligned} \quad (8)$$

where $I_0 = 2A^2 + B^2$.

To show the operation mechanism of the optical Vernier effect, the simulation spectrum of the FIs are displayed in Figure 2a, respectively. The sensing FI corresponds to the red curve, and the reference FI corresponds to the blue curve. At λ_0 , the two FIs are in phase, the peak wavelength $\lambda_s(i)$ of the sensing FI coincides with the peak wavelength $\lambda_r(j)$ of the reference FI, and i and j are orders of the interference peaks. The dip of the Vernier effect envelope appears at the position where two interferometric spectra just overlap with each other, so the dip wavelength of the Vernier effect envelope can be calculated from Equation (8):

$$\lambda_{\text{dip}}(m) = \frac{|(n_{1a}L_{1a} - n_{1b}L_{1b}) - (n_{2a}L_{2a} - n_{2b}L_{2b})|}{2m + 1} \quad (9)$$

Since the FSR of the reference FI (FSR_1) is slightly smaller than that of the sensing FI (FSR_2), interference peaks of the two FIs behind λ_0 will be separated, and at a certain wavelength (λ_1), the peak wavelength of the two FIs will be once again coincide with each other, as shown in Figure 2a. The maximum of the spectral envelope occurs at the wavelength where the sensing interference peak coincides with the reference interference peak, and the minimum (node) of the spectral envelope happens at the wavelength where the sensing interference peak coincides with the reference interference dip. As a result, an optical Vernier effect will be generated owing to the displacement of the two interferometric spectra. The superimposed Vernier effect spectrum of the parallel connected FIs will include periodic envelopes modulated with fine fringes in different intensity, as shown in Figure 2b. The FSR of the envelope can be expressed as:

$$FSR_{\text{envelope}} = \frac{FSR_1 \cdot FSR_2}{|FSR_1 - FSR_2|} \quad (10)$$

It can be easily deduced from Equation (10) that the smaller the variation between the phase difference of the sensing FIs and the reference FIs, the larger the FSR_{envelope} of the Vernier effect spectrum. However, if FSR_2 and FSR_1 are too close, the envelope may be large enough and even exceed the detection range.

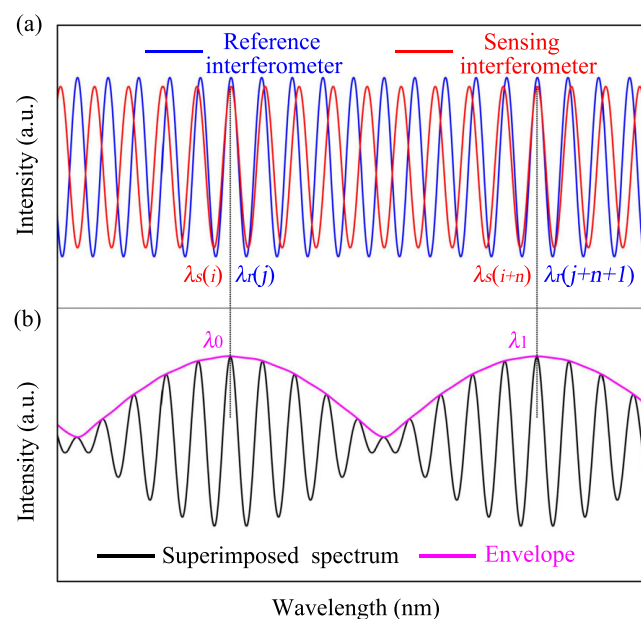


Figure 2. Working mechanism of the optical Vernier effect: (a) spectrum of the sensing and reference FI; (b) superimposed spectrum of the parallel connected FIs.

The magnification factor (M) characterizes the optical Vernier effect. It is an important parameter to connect the Vernier envelope modulation and the individual interferometric fringe. The magnification factor is defined as the ratio between the wavelength shift of the envelope and the wavelength shift of the sensing interferometer [9,10].

If there is a variation of the external sensing parameter, the refractive index or the length of the fiber interferometer will change accordingly, leading to a shift of the interference spectrum. The spectrum shift caused by the change of external environment can be deduced from Equation (4):

$$\Delta\lambda_{\text{dip}1} = \lambda_{\text{dip}1} \left(\frac{\partial n_{1a}}{n_{1a}} + \frac{\partial L_{1a}}{L_{1a}} - \frac{\partial n_{1b}}{n_{1b}} - \frac{\partial L_{1b}}{L_{1b}} \right) \quad (11)$$

$$\Delta\lambda_{\text{dip}2} = \lambda_{\text{dip}2} \left(\frac{\partial n_{2a}}{n_{2a}} + \frac{\partial L_{2a}}{L_{2a}} - \frac{\partial n_{2b}}{n_{2b}} - \frac{\partial L_{2b}}{L_{2b}} \right) \quad (12)$$

Combined with Equation (9), the shift of the Vernier effect envelope can be expressed as:

$$\Delta\lambda_{\text{dip}} = \lambda_{\text{dip}} \frac{(\partial n_{1a}L_{1a} + n_{1a}\partial L_{1a} - \partial n_{1b}L_{1b} - n_{1b}\partial L_{1b}) - (\partial n_{2a}L_{2a} + n_{2a}\partial L_{2a} - \partial n_{2b}L_{2b} - n_{2b}\partial L_{2b})}{|(n_{1a}L_{1a} - n_{1b}L_{1b}) - (n_{2a}L_{2a} - n_{2b}L_{2b})|} \quad (13)$$

If $\lambda_{\text{dip}} = \lambda_{\text{dip}1} = \lambda_{\text{dip}2}$, the wavelength of the Vernier effect envelope dip coincides with that of the two interferometers, so there is $\lambda_{\text{dip}} = \lambda_{\text{dip}1} = \lambda_{\text{dip}2}$. From Equations (11)–(13), we have the relationship between $\Delta\lambda_{\text{dip}}$, $\Delta\lambda_{\text{dip}1}$ and $\Delta\lambda_{\text{dip}2}$:

$$\Delta\lambda_{\text{dip}} = M_1\Delta\lambda_{\text{dip}1} - M_2\Delta\lambda_{\text{dip}2} \quad (14)$$

where M_1 and M_2 are sensitivity magnification factors of the Vernier effect compared to interferometer 1 and interferometer 2.

$$M_1 = \frac{FSR_1}{FSR_1 - FSR_2} = \frac{(n_{2a}L_{2a} - n_{2b}L_{2b}) - (n_{1a}L_{1a} - n_{1b}L_{1b})}{n_{1a}L_{1a} - n_{1b}L_{1b}} \quad (15)$$

$$M_2 = \frac{FSR_2}{FSR_1 - FSR_2} = \frac{(n_{2a}L_{2a} - n_{2b}L_{2b}) - (n_{1a}L_{1a} - n_{1b}L_{1b})}{n_{2a}L_{2a} - n_{2b}L_{2b}} \quad (16)$$

From the above two equations, we know that M_1 and M_2 have the same sign. It can be positive or negative, depending on the value of FSR_1 and FSR_2 .

Figure 3a,b show the case when $FSR_r > FSR_s$. Initially, at λ_0 , the interference peak of the sensing spectrum coincides with that of the reference spectrum. Thus, the envelope peak of the overlap spectrum occurs at λ_0 . If the sensing spectrum redshifts with $\Delta\lambda = FSR_r - FSR_s$, as shown in Figure 3b, the sensing spectrum and the reference spectrum are coincident again at λ_1 . Meanwhile, the peak wavelength of the superimposed spectral envelope also moves to λ_1 . In this case, both the sensing spectrum and the Vernier effect envelope shift to the same direction. Thus, in the case of $FSR_r > FSR_s$, M is positive. Figure 3c,d show the case when $FSR_r < FSR_s$. When the sensing spectrum redshifts with $\Delta\lambda = |FSR_r - FSR_s|$, the peak wavelength of the superimposed spectral envelope blueshifts to λ_{-1} . In this case, M is negative, and the envelope and the individual sensing dip move to opposite directions.

From the above analysis, we can see that through the Vernier effect, the sensitivity could be improved by orders of magnitude. With a detector of determined detection accuracy, the detection resolution of the sensor can be significantly improved. At the same time, we noticed that the Vernier envelope is with a bigger width. To ensure a high detection accuracy, a detector with high wavelength detection accuracy is needed. Otherwise, the detection accuracy will be compromised. Even so, the sensitivity enhancement caused by the Vernier effect still plays a major role in improving the detection accuracy, which could offset the adverse effects of the wide Vernier envelope to a certain extent.

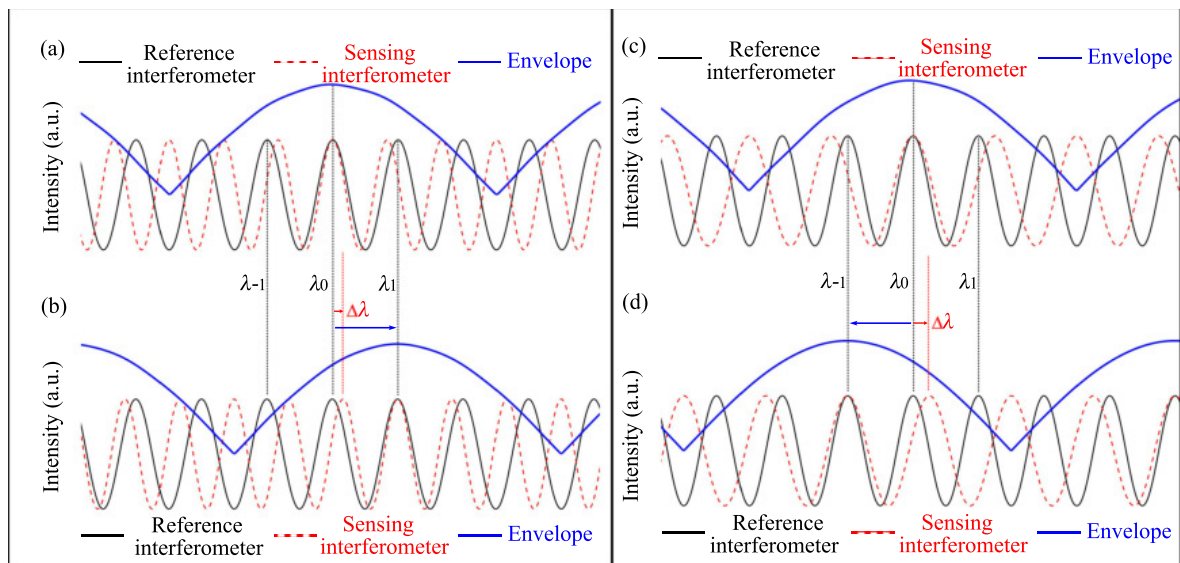


Figure 3. The relationship between the wavelength shift of the Vernier effect envelope and individual spectrum: (a) $FSR_r > FSR_s$, initial spectrum; (b) $FSR_r > FSR_s$, both the sensing spectrum and the Vernier envelope redshift; (c) $FSR_r < FSR_s$, initial spectrum; (d) $FSR_r < FSR_s$, sensing spectrum redshifts, the Vernier effect envelope blue shifts.

3. Configurations to Produce the Vernier Effect

In recent years, many interferometric fiber sensors have been integrated to produce sensitivity-enhanced fiber sensors based on the Vernier effect. This section reviews the configurations of optical fiber sensors with Vernier effect published in recent years, and their advantages and disadvantages are analyzed.

According to the types of distinct fiber sensors, the configurations to produce the Vernier effect can be roughly divided into three categories. The first two categories contain traditional optical fiber interferometers (single type and hybrid type), which can produce the Vernier effect through series or parallel connections, and the third category contains optical fiber sensors with new mechanisms.

Before introducing the constructions of Vernier effect fiber sensors, it should be noted that: (i) all sensitivity values, resolutions and other indexes mentioned in this review are experimental measurement results obtained in the references, (ii) the light sources used in the Vernier effect fiber sensor setups are broadband light sources, mostly cover C-L band. Readers who are interested in the experimental setups should refer to the related references for detailed information. This section mainly focuses on the classification of Vernier effect fiber sensor configurations.

3.1. Configurations Include Single-Type Interferometers

3.1.1. Vernier Effect Fiber Sensors Based on FPIs

To take full advantage of the Vernier effect, a periodic spectrum with fine fringes, stable peak and dip amplitude is necessary. The spectrum of FPI meets the criteria very well. In addition, the reflective structure and compact size make FPI flexible to be applied in many occasions. The typical configurations using FPIs to create the Vernier effect are summarized in Figure 4 [11–13].

One method of integrating FPIs to produce the Vernier effect is to connect two FPIs in parallel, as shown in Figure 4a [11]. The other way is to assemble two FPIs in a series configuration. The FPIs can be physically separated or connected, as shown in Figure 4b,c. Table 1 lists several cases of fiber sensors that combine two FPIs in parallel to realize the Vernier effect, in which the structures, applications, sensitivities and magnification factors are summarized and compared. In the same form, Table 2 summarizes the Vernier-effect-based fiber interferometers that combine FPIs in series.

The parallel-structured FPI fiber sensor with the Vernier effect was first proposed in 2019 by Yao et al. [14]. The authors proposed an ultrasensitive RI sensor based on two parallel connected FPIs with the Vernier effect. The spectrum of the two FPIs was reflected through a 3 dB coupler and then naturally superimposed to produce the Vernier effect. The open and closed cavity FPIs fabricated on the two arms of a 3 dB coupler were used as the sensing and reference units, respectively. NaCl solutions with different RIs could be filled in and drained out from the open cavity FPI. Experimental results showed that by tracing the Vernier effect envelope, a RI sensitivity of 30,801.53 nm/RIU was achieved with RI ranges from 1.33347 to 1.33733, almost 33 times higher than that of the single FPI. After the publication of this paper, a few more Vernier effect fiber sensors with parallel configurations were reported. By introducing a microsphere air cavity FPI [15–17], a polydimethylsiloxane (PDMS)-filled air cavity FPI [18,19], a heterogeneous fiber structured FPI [20] and an open air cavity FPI [11] in the Vernier-effect-based fiber sensors, the measured sensitivity can significantly be improved, as shown in Table 1 [14–16,18–21].

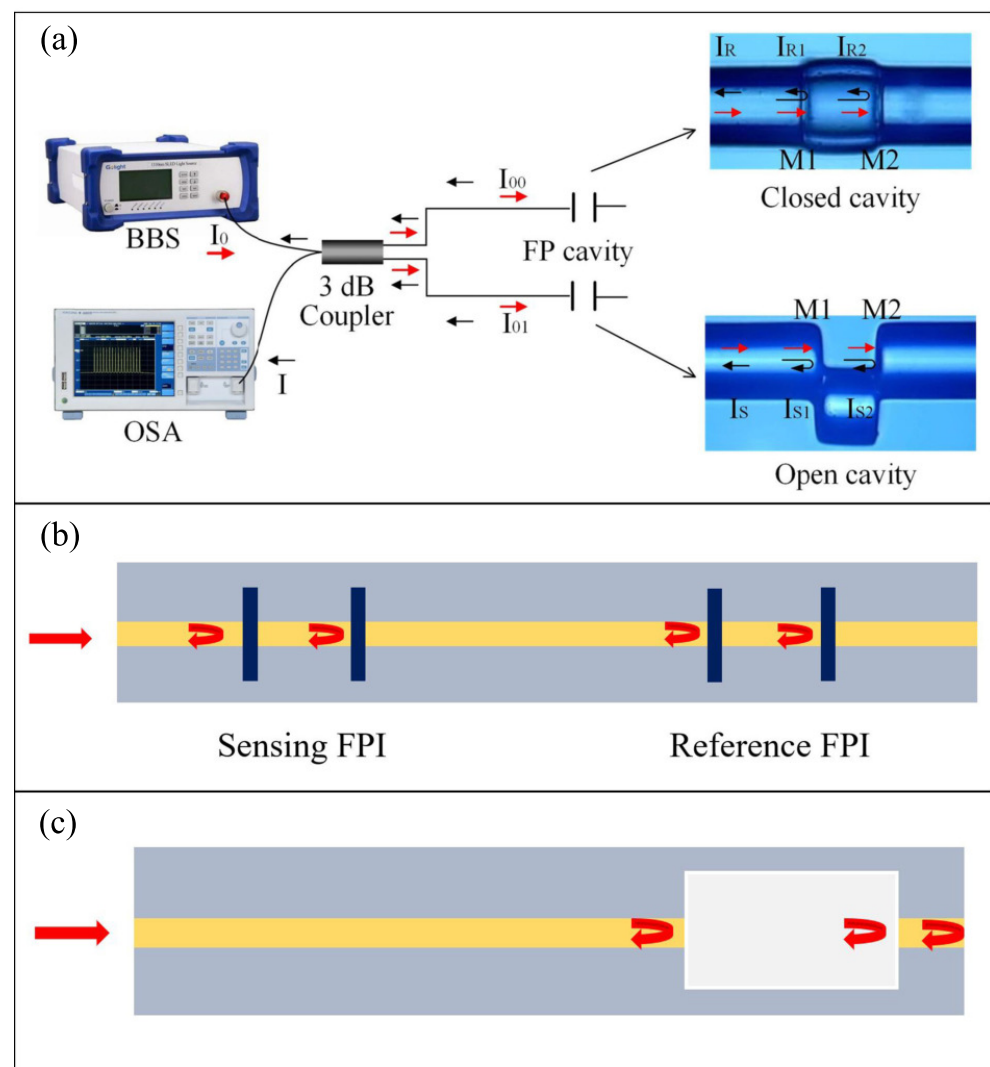


Figure 4. Configurations of Vernier effect fiber sensors based on FPIs: (a) in parallel [11]; (b) in series (physically connected); (c) in series (physically separated). Reprinted with permission from Ref. [11]. ©The Optical Society.

Table 1. Summary of the Paralleled FPI Fiber Sensors with the Vernier Effect.

Configuration	Application	Sensitivity	Testing Range	<i>M</i>	Year	Ref.
Dual FPIs formed by SMF end face and a mirror	RI	30,801.53 nm/RIU	1.33347~1.33733	33	2019	[14]
Dual FPIs constructed by microbubble cavities	Salinity	82.61 nm/m	0~0.297 m	6.83	2019	[15]
Hollow microsphere cavity and Hollow core fiber	Transverse load	-3.75 nm/N	0~0.98 N	3.4	2019	[16]
FPI filled with PDMS and Hollow core fiber	Temperature	17.758 nm/°C	46~50 °C	27.2	2019	[18]
FPI filled with PDMS and FPI covered by ultraviolet glue layer	Pressure & Temperature	-36.93 nm/MPa 10.29 nm/°C	0.1~0.85 MPa 44~49 °C	-	2021	[19]
Dual FPIs constructed by suspended-core fibers	Temperature	153.8 pm/°C	40~220 °C	14.6	2019	[20]
Dual FPIs: SMF and HCF	Strain	53.2 pm/μ ϵ	0~300 μ ϵ	26.6	2021	[21]

There are several advantages of the parallel configurations: (i) The sensing FPI and the reference FPI are physically separated. Consequently, the reference unit can be fully isolated from the measurand, thus keeping a relatively stable interference spectrum. (ii) The FPIs can be fabricated separately, which allows the FPIs to be fabricated in various shapes or materials.

Table 2 lists the cascaded FPI fiber sensors with the Vernier effect. Obviously, compared to the case of paralleled FPIs, the cascaded configurations were the first researched by scholars and thus reported the most. For the cascaded configurations to produce the Vernier effect, the FPIs that are physically separated have advantages similar to those of the paralleled configuration. However, this new configuration has not been fully explored. In 2018, Zhang et al. first proposed an ultrasensitive temperature fiber sensor based on two cascaded FPIs that are physically separated. The sensing FPI is composed of a cleaved fiber end-face and UV-cured adhesive, while the reference FPI is formed by a hollow core fiber (HCF) sandwiched between SMFs [22]. Benefiting from the separated configuration, the sensing and reference FPIs can be flexibly adjusted to meet different application demands. Following this work, several Vernier effect fiber sensors that adopted separated FPIs were reported. For example, the FPIs can be physically separated by a laser-inscribing method [13,23,24]. A schematic diagram of this kind of configuration is depicted in Figure 4b. By using two circulators, the FPIs can also be connected in a series [25]. The circulator scheme makes the sensing and reference FPIs move freely and allows more flexible adjustments to the FPIs. According to the statistical results in Table 2, the scheme of FPIs physically connected was researched the most. A typical configuration of FPIs physically connected to produce the Vernier effect is shown in Figure 4c. For example, the FPI could be formed by splicing a section of HCF between a lead-in SMF and a short SMF section. In Ref. [12], the sensor was applied to measure the airflow. The highest airflow velocity sensitivity of the sensor reached 1.541 nm/(m/s) in the region of 3~7 m/s. In addition, many schemes similar to this structure have been reported, most of which combine the air cavity and the silica cavity to produce the Vernier effect [10,12,26–40]. There are also some reports that employ the air cavity and the other cavity together [41,42].

Table 2. Summary of the Cascaded FPI Fiber Sensors with the Vernier Effect.

Configuration	Application	Sensitivity	Testing Range	<i>M</i>	Year	Ref.
SMF + PCF + HCF+ Graphene Quantum Dots	Humidity	0.456 nm/%RH	19.63~78.86%	4.8	2019	[10]
SMF + HCF + SMF	Airflow	1.541 nm/(m/s)	3~7 m/s	9.57	2016	[12]
Laser-inscribed mirrors in SMF	Strain	28.11 pm/ $\mu\epsilon$	0~1500 $\mu\epsilon$	-	2019	[13]
SMF + HCF + SMF + NOA65 filled ceramic ferule	Temperature	67.35 nm/ $^{\circ}\text{C}$	20~24 $^{\circ}\text{C}$	23.41	2018	[22]
Laser-inscribed mirrors in SMF	Strain	145 pm/ $\mu\epsilon$	0~200 $\mu\epsilon$	-	2019	[23]
Laser-inscribed mirrors in SMF	temperature & strain	(1050 \pm 20) pm/ $^{\circ}\text{C}$ (113 \pm 2) pm/ $\mu\epsilon$	30~70 $^{\circ}\text{C}$ 0~600 $\mu\epsilon$	-	2021	[24]
closed FP cavity + open FP cavity	Gas RI	-16,335.96 nm/RIU	1.0000266~1.0002663 RIU	11.12	2019	[25]
SMF + HCF + coated LMAF	Hydrogen	-1.04 nm/%	0~2.4 %	-	2018	[26]
SMF + side opened HCF + SMF	Gas Pressure	80.3 pm/kPa	100~300 kPa	20	2019	[27]
SMF + Simplified HCF + SMF	Temperature	1.019 nm/ $^{\circ}\text{C}$	250~300 $^{\circ}\text{C}$	-	2015	[28]
SMF + HCF + PCF	Gas refractive index	30,899 nm/RIU	1.00277~1.00372 RIU	-	2015	[29]
SMF + HCF + SMF column + hollow fiber ball	Temperature	-1.081 nm/ $^{\circ}\text{C}$	30~42 $^{\circ}\text{C}$	-	2018	[30]
SMF + air gap + SMF with fusion hole	Gas pressure	86.64 nm/MPa	0~0.6 MPa	32.8	2018	[31]
SMF + LCs + SMF coated with gold film	Temperature	19.55 nm/ $^{\circ}\text{C}$	23~31 $^{\circ}\text{C}$	-	2018	[32]
SMF + microhole cavity + SMF section	RI & Temperature	1143.0 nm/RIU -0.1805 nm/ $^{\circ}\text{C}$	1.3352~1.3469 RIU 30~90 $^{\circ}\text{C}$	-	2019	[33]
SMF + HCF + LMAF	Isopropanol	20 pm/ppm	0~500 ppm	-	2019	[34]
SMF + PMPCF + HCPCF + MMF	Temperature	535.16 pm/ $^{\circ}\text{C}$	24~1000 $^{\circ}\text{C}$	45	2019	[35]
SMF + HCF filled with DSO + UV glue	Temperature	39.21 nm/ $^{\circ}\text{C}$	34.3~36.1 $^{\circ}\text{C}$	27	2020	[36]
SMF + silica tube + hole-assisted one-core fiber	Gas RI	-9462.4 nm/RIU	1.00003~1.00048	6.8	2021	[39]
Air cavity + silica microsphere	Displacement	344.8 pm/nm	0~4 μm	-	2021	[40]
SMF + air gap + chitosan cavity	Humidity	7.15 nm/% RH	40~92% RH	-	2021	[41]
air cavity + PDMS cavity	Temperature	4.7 nm/ $^{\circ}\text{C}$	35~45 $^{\circ}\text{C}$	-	2021	[42]

3.1.2. Vernier Effect Fiber Sensors Based on MZIs

To produce the Vernier effect, some scholars assemble different typed MZIs together. Similar to the case of FPIs employed to introduce the Vernier effect, the MZIs can be assembled in cascade [9,43–45] or in parallel [46–50]. As depicted in Figure 5a, for the cascaded inline structures, the two MZIs can be physically connected [45–51] or separated by a section of SMF [9,43,44]. For the paralleled structures, MZIs can be assembled by two 3 dB couplers [50] or integrated into a single fiber by micromachining [46–49], shown in Figure 5b.

The MZIs in series just need to cascade traditional fiber MZIs together, separated or connected. Many special structures have been reported for the constitution of in-line MZIs, such as offset splicing [9], spherical structure [43], few-mode fiber [44] and so on. In 2017, Liao et al. proposed a sensitivity-amplified Vernier effect fiber sensor, which is based on two cascaded MZIs formed by offset splicing [9]. The experimental setup of the sensing system is shown in Figure 6. Using one MZI as a reference and the other as a sensor, this Vernier effect fiber sensor is applied to temperature and curvature sensing. Temperature sensitivity of the sensor under a modified Vernier effect is about 397.36 pm/ $^{\circ}\text{C}$, with a *M* factor of 8.7. For curvature sensing, the sensitivity is enhanced from -4.55 nm/m⁻¹ to about -36.26 nm/m⁻¹, with a *M* factor of ~8. To make the sensor more compact, MZIs can also be physically connected by micromachining [45,51].

To simplify the manufacturing process of MZIs, an efficient way is to employ few-mode fiber (FMF). In 2020, two SMF–FMF–SMF structures were cascaded to carry out pressure sensing, where the FMF was specially designed and only supported LP01 and LP02 modes [44]. In the superimposed interferometric spectrum of this sensor, envelopes

with changing FSRs and a critical wavelength of the envelope could be observed. By extracting the peaks of the envelope located near the critical wavelength of the envelope, a static pressure sensitivity of 4.072 nm/MPa in a pressure range of 0–3 MPa was reported. This paper proposed an effective way to employ the Vernier effect. Pure modal interference could be obtained in FMF only by the simplest splicing, but the disadvantage is that customized FMF increases the cost. As an recent alternative, cascaded fiber tapers were extensively used to produce the Vernier effect [52–54]. The cascaded fiber tapers conformed to a pair of MZIs. By tapering, higher order modes were excited in the waist region, and when they recoupled back to the fiber, interference occurred.

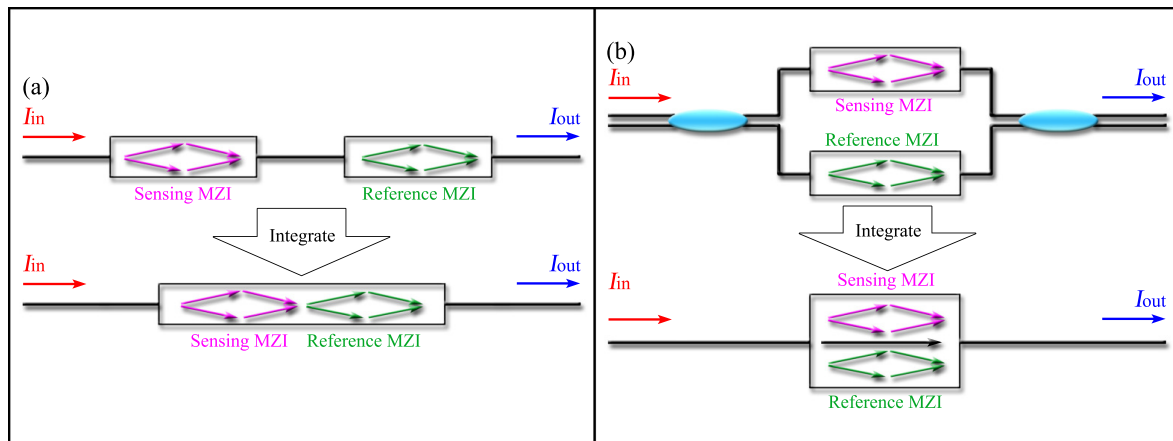


Figure 5. Vernier effect fiber sensor with: (a) cascaded MZIs; (b) parallel connected MZIs.

The simplest way to produce the Vernier effect by connecting two MZIs in parallel is to connect MZIs with two 3 dB couplers [50]. To simplify the structure, the researchers integrated the parallel structure into one fiber [46–49]. As a representative, in 2018, Lin et al. proposed a gas pressure sensor based on dual side-hole fiber (DSHF) interferometers with the Vernier effect [47]. The sensor is composed of two integrated parallel MZIs formed by splicing a short section of DSHFs between two short pieces of MMFs. To introduce the Vernier effect, a femtosecond laser is applied to cut off part of the MMF and drill openings on one air hole of the DSHF. A high gas pressure sensitivity of -60 nm/MPa was achieved in the range of 0~0.8 MPa.

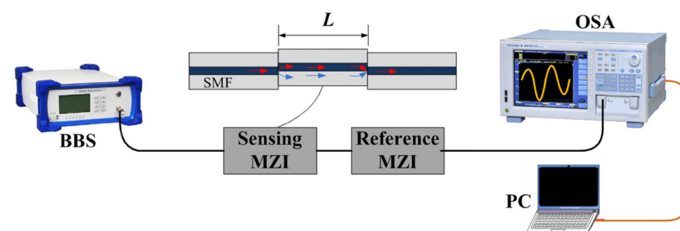


Figure 6. Experimental setup of the cascaded in-line MZIs [9]. Reprinted with permission from Ref. [9] ©The Optical Society.

Compared to FPIs, the cascaded MZIs are transmissive configurations. Considering the practical measuring applications, the light source and the interrogator should be distributed at both ends of the MZI sensor, which is inconvenient in the operating process.

3.1.3. Vernier Effect Fiber Sensors Based on MIs

The principle of MI is similar to MZI. Both interferometers accumulate optical path difference by dividing light into two paths. The light is then combined together to produce interference. The difference is that the MZI is a transmissive structure, and MI is a reflective structure. Light propagates to the MI end and is then reflected along the same path.

Employing some special fibers, such as multicore fiber, DSHF, etc., scholars have proposed some schemes to implement miniaturized Vernier effect fiber sensors based on MIs. In 2018, Zhang et al. reported a curvature sensor that consisted of a pair of juxtaposed MIs [55]. With curvature applied to the triple-core fiber, a small RI difference occurs between the eccentric cores. Finally, the optical path difference of the three paths contributes to the optical Vernier effect. The Vernier envelope showed a high curvature sensitivity with a low temperature crosstalk. The next year the same research group reported another Vernier effect fiber sensor with parallel fiber MIs for bending sensing [56]. The sensor consists of an asymmetric dual-core fiber and a short section of DSHF, as shown in Figure 7a. The centric core of the dual-core fiber is spliced to the DSHF with a little lateral offset, so light can be coupled to both the core and cladding of the DSHF. Three light beams reflected from the core and cladding of the DSHF and the eccentric core of the dual-core fiber interfere with each other, forming two parallel MIs. Experiments showed a bending sensitivity of 38.53 nm/m^{-1} from $0 \sim 1.24 \text{ m}^{-1}$ by demodulating the Vernier envelope. Later in 2020, Li et al. proposed a curvature sensor, which consists of a pair of parallelized dual-core fiber MIs, shown in Figure 7b [57]. This sensor achieved a curvature sensitivity of $214.533 \text{ nm/m}^{-1}$ with a low temperature crosstalk.

3.1.4. Vernier Effect Fiber Sensors Based on Fiber Loop Mirrors

Normally, a Sagnac interferometer can be fabricated by connecting two transmission ports of a 3dB coupler. By inserting a section of high-birefringent (Hi-Bi) fiber in between the Sagnac loop, a fiber loop mirror (FLM) is formed. The input light is split equally into two beams through the fiber coupler, and the two beams travel through the fiber loop in opposite directions. Due to the birefringence effect of the Hi-Bi fiber, the two counterpropagating beams further decompose into two orthogonal linearly polarized wave components when they enter the Hi-Bi fiber. The OPD is accumulated during the propagating process. At the output port, the two beams recombine, and the interference spectrum occurs. Usually, a polarization controller is adopted to adjust the fringe visibility of the spectrum. The FLM is an important device in the fiber sensing area and has attracted considerable research efforts. To further improve the sensing sensitivity of FLMs sensors, some researchers have cascaded FLMs, which have almost the same FSRs, and amplified sensitivities were achieved through the Vernier effect.

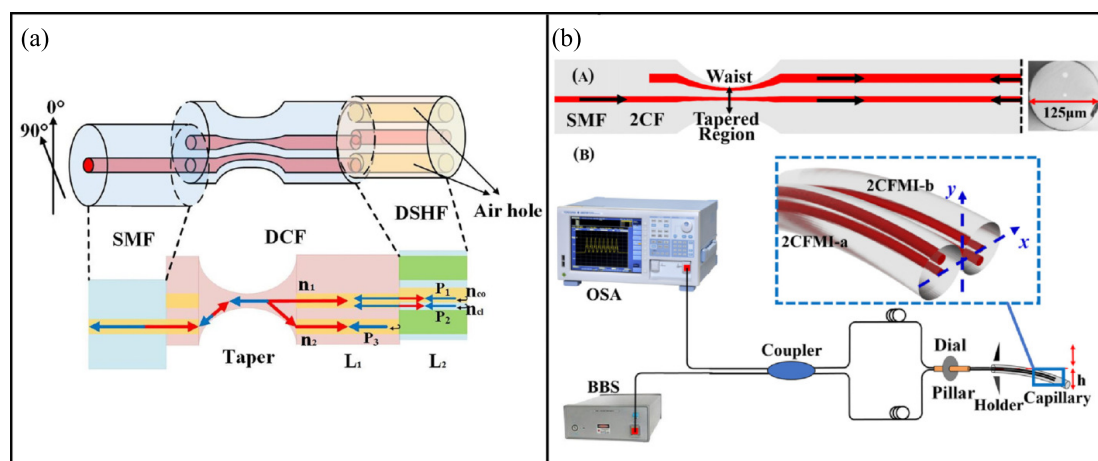


Figure 7. Schematic diagrams of the Vernier effect fiber sensors based on parallelized MIs, (a) the sensor consists of an asymmetric dual-core fiber and a short section of DSHF [56], (b) the sensor consists of a pair of parallelized dual-core fiber MIs [57], (A) the sensor probe, (B) the schematic diagram of experimental system. Reprinted with permission from Ref. [56] ©Elsevier. Reprinted with permission from Ref. [57] ©The Optical Society.

In 2015, Shao et al. proposed a highly sensitive temperature fiber sensor that employed the Vernier effect by cascading two FLMs [58]. The typical configuration is presented in Figure 8a. By tracing the Vernier envelope, a temperature sensitivity of $-13.36 \text{ nm}/^\circ\text{C}$ was achieved, with a M factor of ~ 9 . In 2021, the same scheme was adopted for strain measurement [59]. Using a similar scheme, a special case of a harmonic Vernier effect was reported and applied to strain measurement [60]. The authors used harmonics of the Vernier effect to further increase the sensitivity, and strain sensitivities of $(80.0 \pm 0.3) \text{ pm}/\mu\epsilon$ for the fundamental Vernier envelope and $(120 \pm 1) \text{ pm}/\mu\epsilon$ for the Vernier envelope of the first harmonic were achieved. Later, this scheme was again demonstrated for temperature sensing by Liu et al., and an enhanced temperature sensitivity of $3.66 \text{ nm}/^\circ\text{C}$ was obtained [61]. The harmonic Vernier effect will be further discussed in Section 3.3.

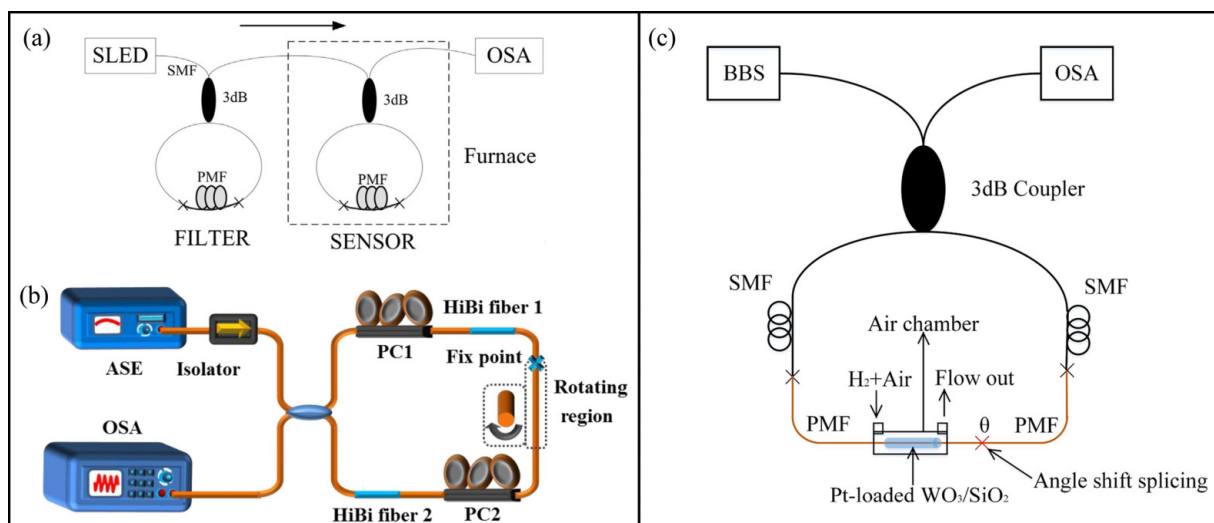


Figure 8. Vernier effect fiber sensor formed by (a) cascading two FLMs [58], (b) inserting two Hi-Bi fiber segments into a fiber loop [62], (c) angle shift-splicing two Hi-Bi fibers in a single Sagnac loop [63]. Reprinted with permission from Refs. [58,63] ©Elsevier.

In 2016, a compact configuration based on FLM to produce the Vernier effect was proposed. Two Hi-Bi fiber segments were inserted into the fiber loop, as shown in Figure 8b [62]. Temperature and torsion sensing were experimentally demonstrated. An enhanced temperature sensitivity of $-17.99 \text{ nm}/^\circ\text{C}$ and a M factor of ~ 12 were achieved. Additionally, the external torsion and the fringe visibility perfectly conformed to the Sine relationship over a 360° twist angle. In 2018, Wu et al. proposed a similar fiber sensor based on the Vernier effect and demonstrated for temperature and hydrogen sensing [63]. The Vernier effect was achieved by angle shift-splicing Hi-Bi fibers in a single Sagnac loop, as shown in Figure 8c.

The experimental results showed an enhanced temperature sensitivity of $-2.44 \text{ nm}/^\circ\text{C}$ with a M factor of 14.96 and an enhanced hydrogen sensitivity of $-14.61 \text{ nm}/\%$ (in the range of 0–0.8%) with a M factor of 1.85. Later, similar structures were demonstrated to realize simultaneous strain and temperature [64] and isopropanol measurement [65].

3.1.5. Vernier Effect Fiber Sensors Based on Microfiber Couplers

Fiber couplers have been widely applied in the field of fiber communication. In fact, it can also be used for fiber sensing. Compared to other Vernier effect fiber sensors that assemble different interferometers together, the optical microfiber coupler (OMC) is easy to be fabricated and is highly sensitive to measurands, which is a promising candidate to be applied in areas that require high sensitivity.

In 2018, Li et al. first reported the scheme of using OMC to produce the Vernier effect and further applied it to sensitivity enhancement [66]. Figure 9 shows the schematic structure and the working principle of a typical OMC. The coupling region of the OMC is highly birefringent. It consists of two parallel and neighboring microfibers. The x -polarized interference and the y -polarized interference vary slightly. As they superimpose at the output port, the Vernier effect would be produced. The OMC was first applied to measure RI, and an enhanced RI sensitivity of 35,823.3 nm/RIU was achieved. The authors further applied this structure to detect human cardiac troponin, and a detection limit of 1 ng/mL was reported. Similarly, Chen et al. proposed a Vernier effect double helix microfiber coupler to enhance the RI sensitivity. With the minimum coupler diameter of 3.4 μm , the achieved RI sensitivity was up to 27,326.59 nm/RIU in the range of 1.3333–1.3394 [67].

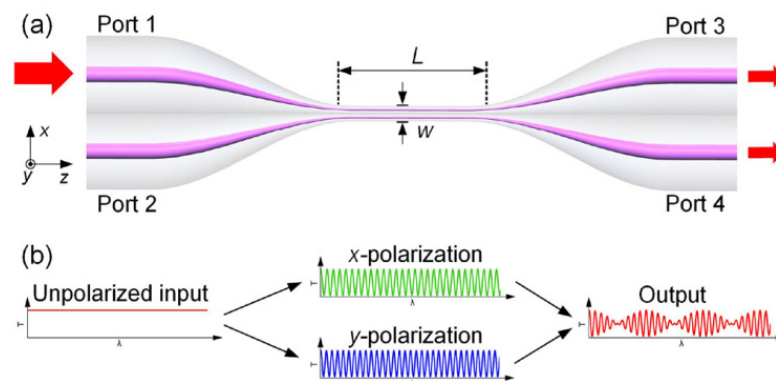


Figure 9. (a) Schematic diagram of the OMC. (b) Vernier effect operation principle of the OMC [66]. Reprinted with permission from Ref. [66] ©Elsevier.

Furthermore, Pengfei Wang's research group explored the mechanism of connecting two couplers together to produce the Vernier effect, as shown in Figure 10 [68]. They first explored the schemes of combining couplers in series and in parallel. By comparison, the couplers in parallel connection have clearer envelope edges. They then applied the dual microfiber couplers for RI sensing, and an ultrahigh sensitivity of 126,540 nm/RIU was achieved in the range of 1.3350–1.3455. Later, they employed the paralleled OMCs for ethanol gas sensing [69]. A mixture of Nile red and polymethyl methacrylate which is sensitive to ethanol gas, was coated on the waist region of the coupler, and the sensor showed a high responsivity of 160 pm/ppm for ethanol gas sensing.

3.1.6. Vernier Effect Fiber Sensors Based on Microfiber Knot Resonators (MKRs)

Sensors based on micro/nanofiber with diameters of a few micrometers are competitive due to their characteristics of high evanescent field fraction, good flexibility and low bending loss. Early in 2013, Vanessa Zamora et al. used two cascaded MKRs for highly sensitive RI sensing [70]. Later, in 2015, Xu et al. proposed a kind of Vernier effect fiber sensor based on MKRs. In their configuration, two MKRs [71] were cascaded in series through a bus microfiber, as shown in Figure 11. In the experiment, two MKRs with similar radii (1.178 mm and 1.230 mm) were cascaded, One served as a reference immersed in water with RI kept at 1.3315, while the other served as the sensor with ambient RI increased gradually from 1.3315 to 1.3349. By tracing the Vernier effect envelope, RI sensitivity 6523 nm/RIU was reported between 1.3315 and 1.3349 RIU.

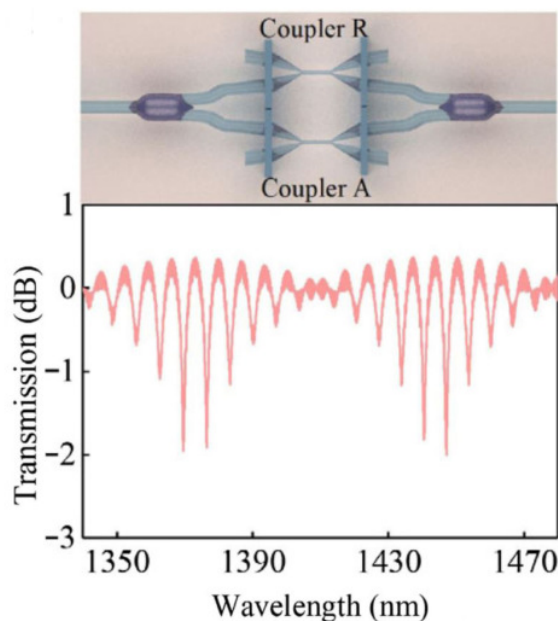


Figure 10. Microfiber couplers connected in parallel to produce the Vernier effect [68]. Reprinted with permission from Ref. [68] ©The Optical Society.

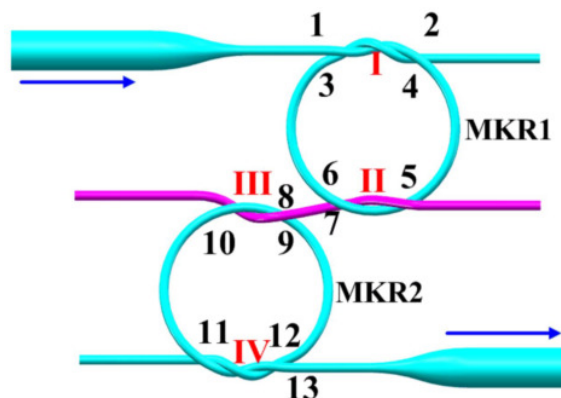


Figure 11. Configuration of cascaded microfiber knot resonators [71]. Reprinted with permission from Ref. [71] ©The Optical Society.

3.2. Configurations Include Hybrid-Type Interferometers

The aforementioned sensors are based on the same type of fiber interferometers. Assembling different kinds of fiber interferometers together can also produce the Vernier effect to enhance the sensing sensitivity. Table 3 summarizes the detailed information of Vernier effect fiber sensors based on hybrid interferometers.

Table 3. Summary of the Vernier effect fiber sensors based on hybrid interferometers.

Configuration	Application	Sensitivity	Testing Range	M	Year	Ref.
MZI and FPI	Temperature	−107.2 pm/°C	30~80 °C	89	2019	[72]
MZI and FPI	RI	−87,261.06 nm/RIU	1.332~1.334	-	2020	[73]
SI and FPI	Temperature	−29.0 nm/°C	42.2~43 °C	20.7	2017	[74]
SI and FPI	Acoustic	37.1 nm/Pa	62.2~92.4 dB	10	2019	[75]
SI and MZI	strain	65.71 pm/με	0~300 με	20	2019	[76]

3.2.1. Hybrid-Type of FPI and MZI

Combining a FPI and a MZI to introduce the Vernier effect was reported by Ying et al. in 2019 [72]. The schematic diagram of the sensor is shown in Figure 12. The FPI is cascaded with MZI through a 2×1 3 dB coupler. The FPI is fabricated by splicing a segment of HCF between SMFs, and the MZI is formed by two 3 dB couplers. The two interferometers have similar FSRs, which results in the Vernier effect. Taking FPI as temperature sensor and MZI as a reference, an enhanced temperature sensitivity of $-107.2 \text{ pm}/^\circ\text{C}$ and M factor of 89 were obtained. The next year, Li et al. proposed an ultrasensitive RI Vernier effect fiber sensor based on cascaded FPI and MZI [73]. Both the FPI and MZI were made up of core-offset structures, as shown in Figure 12b. Different from the traditional Vernier effect fiber sensors that use one interferometer as a sensor and the other as a reference, in this work, both the MZI and FPI were used as sensing elements, resulting in the interference fringes of the MZI and FPI shifting to opposite directions with RI changes and to the same directions as the temperature changed. Therefore, the sensor could magnify RI sensitivity and reduce temperature crosstalk. An ultrahigh RI sensitivity of $-87,261.06 \text{ nm}/\text{RIU}$ was obtained near 1.33, while the temperature sensitivity was only $204.7 \text{ pm}/^\circ\text{C}$.

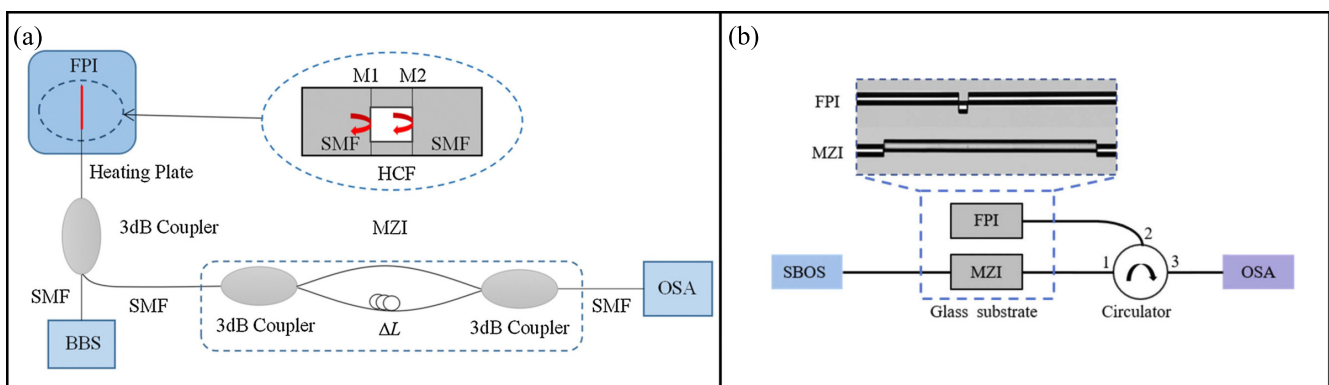


Figure 12. Vernier effect fiber sensors based on hybrid configurations (MZI and FPI), (a) the FPI is fabricated by splicing a segment of HCF between SMFs, and the MZI is formed by two 3 dB couplers [72], (b) both the FPI and MZI were made up of core-offset structures [73]. Reprinted with permission from Ref. [72] ©Elsevier. Reprinted with permission from Ref. [73] ©The Optical Society.

3.2.2. Hybrid-Type of FPI and SI

In 2017, Yang et al. firstly proposed a hybrid SI and FPI Vernier effect sensor to enhance the temperature sensitivity [74]. The SI and FPI were cascaded via a 3 dB fiber coupler and a fiber circulator, as shown in Figure 13. The sensor was employed for temperature sensing, and the temperature sensitivity was enhanced from $-1.4 \text{ nm}/^\circ\text{C}$ to $-29.0 \text{ nm}/^\circ\text{C}$ with a M factor of 20.7. In 2019, Wang et al. adopted a similar configuration for acoustic sensing [75]. The FPI was used as the sensing element, and the FPI cavity length was designed to be adjustable to meet different occasions. At the front of the FPI, a PET film was fixed. When sound pressure of the acoustic signal was applied on the film, phase change was introduced to the FPI. By demodulating the spectrum drift of the Vernier effect envelope, the acoustic signal could be measured. Finally, a maximum sensitivity of $37.1 \text{ nm}/\text{Pa}$ with sound pressure range of $62.2\sim 92.4 \text{ dB}$ was reported.

3.2.3. Hybrid-Type of MZI and SI

In 2019, Liu et al. proposed a Vernier effect strain sensor by cascading a SI and an MZI together, as shown in Figure 14 [76]. The SI comprised a length of PMF and served as the reference part. A MZI fabricated by splicing a section of FMF and SMF together with a slight core-offset to excite the modal interference served as the sensing part. By closing the FSRs of the SI and MZI, the Vernier effect could be produced. Tracing the envelope of the Vernier effect, a high strain sensitivity of $65.71 \text{ pm}/\mu\epsilon$ was reported, with a M factor

of ~ 20 . In 2021, by cascading two three-port couplers to form a MZI, Jia et al. proposed a hybrid structured fiber temperature sensor exploiting the Vernier effect [77].

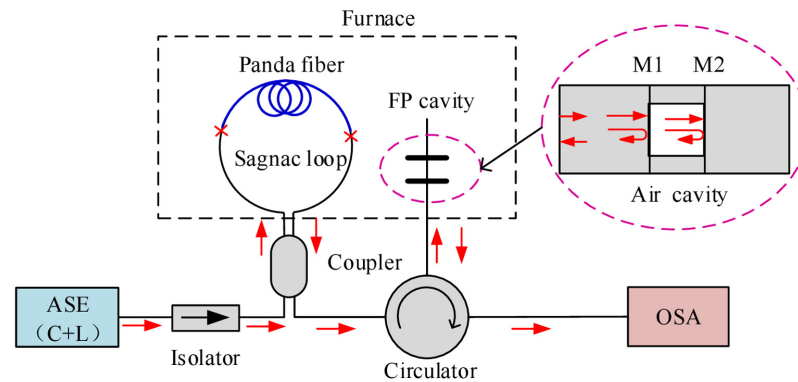


Figure 13. Vernier effect fiber sensor based on hybrid configuration (SI and FPI) [74]. Reprinted with permission from Ref. [74] ©The Optical Society.

Some other Vernier effect fiber sensors based on hybrid interferometers have also been reported, such as θ -shaped microfiber resonator and FPI [78], MZI and MKR [79] and MI and FPI [80] Vernier effect fiber sensors.

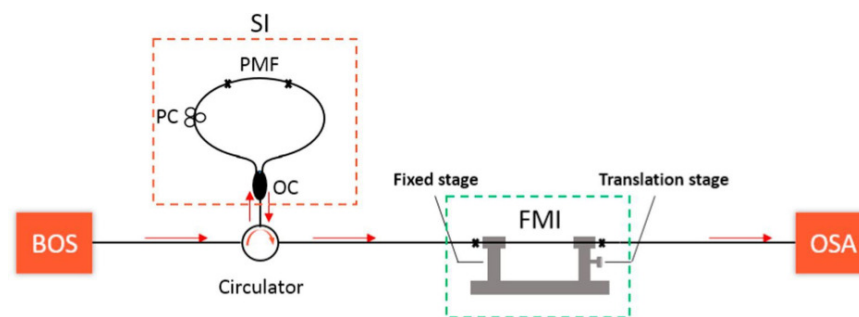


Figure 14. Vernier effect fiber sensor based on hybrid configuration (SI and MZI) [76]. Reprinted with permission from Ref. [76] ©Elsevier.

3.3. Advanced Concepts of Optical Vernier Effect: Optical Harmonic Vernier Effect

Recently, Gomes et al. creatively introduced an advanced concept of a harmonic Vernier effect to further surpass the limits of the conventional Vernier effect [8]. Compared to the conventional Vernier effect, it allows a considerable sensitivity improvement and more flexible control of the sensitivity magnification factor.

In [8], two FPIs connected in parallel through a 3dB fiber coupler were used to demonstrate the optical harmonic Vernier effect. Different from the conventional optical Vernier effect, interferometers can possess very different optical path lengths. As is depicted in Figure 15, the reference FPI has a length of $L_2 + iL_1$, and the sensing FPI has a fixed length of L_2 , i denotes the order of the harmonic, and L_1 is the detuning length. The first case in Figure 15 corresponds to the fundamental optical Vernier effect, where $i = 0$. The following three cases correspond to the first three harmonics ($i = 1, 2, 3$), respectively.

Figure 16 shows the numerical simulations of the fundamental Vernier effect and the first three harmonic orders [8]. The FSR of the internal envelope varies with the order of the harmonic Vernier effect, and the FSR of the i -th harmonic Vernier envelope is $i+1$ times that of the fundamental Vernier effect envelope. The FSR of the i -th harmonic Vernier envelope can be expressed as [8]:

$$FSR_{\text{internalevelope}}^i = \left| \frac{(i+1)FSR_1 FSR_2^i}{FSR_1 - (i+1)FSR_2^i} \right| = (i+1)FSR_{\text{envelope}}^i \quad (17)$$

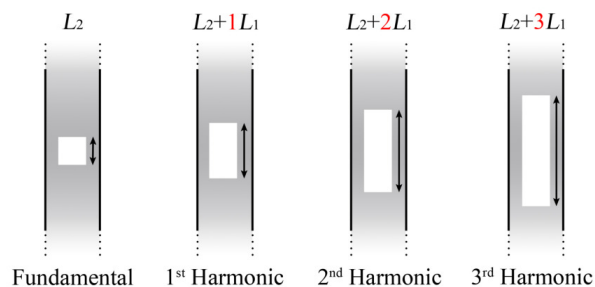


Figure 15. Schematic diagram of the relationship between the length of the reference interferometer ($L_2 + iL_1$) and the sensing interferometer (L_1), where i corresponds to the order of the harmonic [8].

The M -factor for the i -th optical harmonic Vernier effect is $i + 1$ times the magnification of the fundamental optical Vernier effect. A general form of the M -factor is given as [8]:

$$M^i = \frac{FSR_{\text{internal envelope}}^i}{FSR_1} \left| \frac{(i+1)FSR_2^i}{FSR_1 - (i+1)FSR_2^i} \right| = (i+1)M \quad (18)$$

According to Equation (18), the M -factor increases linearly with the harmonic orders. The optical harmonic Vernier effect allows effective control over the M -factor, which can be applied flexibly according to specific needs. Following this work, a few works utilizing optical harmonic Vernier effect were later reported for the measurement of strain [60], temperature [61,81] and gas pressure [38]. The optical harmonic Vernier effect is a promising way to enhance the sensing ability of fiber sensors.

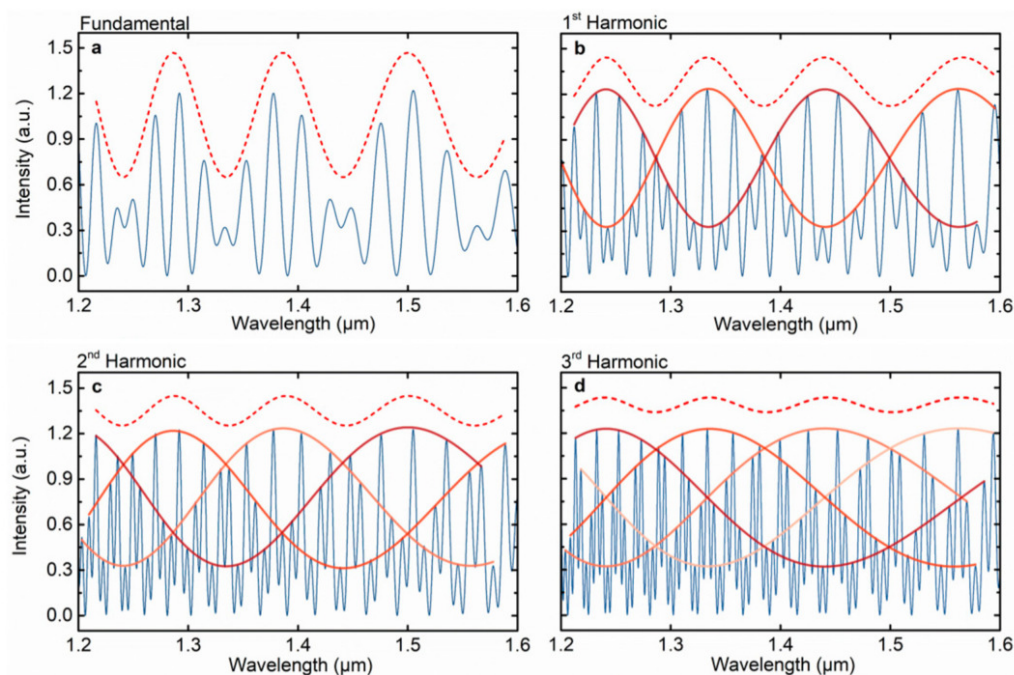


Figure 16. Numerical simulations of the fundamental Vernier effect (a), and the first three harmonic orders (b–d) [8]. Blue line: Simulations of the Vernier effect spectra. Dashed line: Upper envelope (shifted upward to be distinguishable from the internal ones). Red-orange lines: Internal envelopes.

4. Conclusions

This paper reviews different configurations to produce the optical Vernier effect. According to their intrinsic characteristics, the configurations are classified into several categories. Different methods to produce the Vernier effect are compared and discussed, and the indexes are listed for some cases.

The optical Vernier effect could enhance the sensitivity of fiber sensors. By matching the FSRs of two fiber interferometers, the sensitivity of individual fiber sensors could be enhanced significantly. Generally, the closer the FSRs of the two fiber interferometers, the larger the magnification factor is. However, there is a trade-off between the magnification factor and the Vernier envelope. A larger magnification factor will lead to a large Vernier effect envelope, and large envelopes are difficult for accurate detection. Thus, in practice, there is an upper limit to the magnification factor.

To break this limitation, the optical harmonic Vernier effect provides a relatively effective solution method. In the operation mechanism, multiple magnification factors are allowed. With this, the sensitivity of fiber sensors can feasibly be tuned according to specific application occasions. Fiber sensors based on a harmonic Vernier effect have long-term prospects in the future development, and they have huge potential to be applied in many aspects of our life.

The combination of the Vernier effect and traditional fiber interferometer is an innovation in the field of sensing. At present, Vernier effect sensors used for measuring physical quantities such as temperature, strain and magnetic field have been reported extensively, and many explorations have been carried out in the field of biochemistry, all of which have achieved high detection accuracy. Optical fiber sensors based on the Vernier effect have become a competitive candidate in the field of sensing measurement, and this kind of sensor is expected to be widely used in the field of precision measurement, such as the field of aerospace, seismic detection, military detection, environmental monitoring, and so forth.

Author Contributions: Conceptualization, L.Z.; software, Y.C. and S.H.; formal analysis, Y.C.; investigation, S.H.; writing—original draft preparation, L.Z.; writing—review and editing, J.T. All authors have read and agreed to the published version of the manuscript.

Funding: This work was funded by National Natural Science Foundation of China under grant number 62105279, 62065001.

Institutional Review Board Statement: Not applicable.

Informed Consent Statement: Not applicable.

Data Availability Statement: Not applicable.

Acknowledgments: The authors would like to acknowledge Enming Zhao for the financial support to this work.

Conflicts of Interest: The authors declare no conflict of interest.

References

1. Miliou, A. In-Fiber Interferometric-Based Sensors: Overview and Recent Advances. *Photonics* **2021**, *8*, 265. [[CrossRef](#)]
2. Rao, Y.J. Recent progress in fiber-optic extrinsic Fabry–Perot interferometric sensors. *Opt. Fiber Technol.* **2006**, *12*, 227–237. [[CrossRef](#)]
3. Zhao, Y.; Zhao, H.; Lv, R.Q.; Zhao, J. Review of optical fiber Mach–Zehnder interferometers with micro-cavity fabricated by femtosecond laser and sensing applications. *Opt. Lasers Eng.* **2019**, *117*, 7–20. [[CrossRef](#)]
4. Culshaw, B. The optical fibre Sagnac interferometer: An overview of its principles and applications. *Meas. Sci. Technol.* **2005**, *17*, R1. [[CrossRef](#)]
5. Lee, B.H.; Kim, Y.H.; Park, K.S.; Eom, J.B.; Kim, M.J.; Rho, B.S.; Choi, H.Y. Interferometric fiber optic sensors. *Sensors* **2012**, *12*, 2467–2486. [[CrossRef](#)] [[PubMed](#)]
6. Liu, Y.; Li, X.; Zhang, Y.N.; Zhao, Y. Fiber-optic sensors based on Vernier effect. *Measurement* **2021**, *167*, 108451. [[CrossRef](#)]
7. Gomes, A.D.; Bartelt, H.; Frazão, O. Optical Vernier Effect: Recent Advances and Developments. *Laser Photonics Rev.* **2021**, *15*, 2000588. [[CrossRef](#)]
8. Gomes, A.D.; Ferreira, M.S.; Bierlich, J.; Kobelke, J.; Rothhardt, M.; Bartelt, H.; Frazão, O. Optical harmonic Vernier effect: A new tool for high performance interferometric fiber sensors. *Sensors* **2019**, *19*, 5431. [[CrossRef](#)]
9. Liao, H.; Lu, P.; Fu, X.; Jiang, X.; Ni, W.; Liu, D.; Zhang, J. Sensitivity amplification of fiber-optic in-line Mach–Zehnder Interferometer sensors with modified Vernier-effect. *Opt. Express* **2017**, *25*, 26898–26909. [[CrossRef](#)] [[PubMed](#)]
10. Zhao, Y.; Tong, R.J.; Chen, M.Q.; Peng, Y. Relative humidity sensor based on Vernier effect with QODs-PVA un-fully filled in hollow core fiber. *Sensors Actuators A Phys.* **2019**, *285*, 329–337. [[CrossRef](#)]

11. Nan, T.; Liu, B.; Wu, Y.; Wang, J.; Mao, Y.; Zhao, L.; Sun, T.; Wang, J. Ultrasensitive strain sensor based on Vernier-effect improved parallel structured fiber-optic Fabry-Perot interferometer. *Opt. Express* **2019**, *27*, 17239–17250. [[CrossRef](#)]
12. Zhao, Y.; Wang, P.; Lv, R.; Liu, X. Highly sensitive airflow sensor based on Fabry-Perot interferometer and Vernier effect. *J. Light. Technol.* **2016**, *34*, 5351–5356. [[CrossRef](#)]
13. Deng, J.; Wang, D. Ultra-sensitive strain sensor based on femtosecond laser inscribed in-fiber reflection mirrors and Vernier effect. *J. Light. Technol.* **2019**, *37*, 4935–4939. [[CrossRef](#)]
14. Yao, T.; Pu, S.; Zhao, Y.; Li, Y. Ultrasensitive refractive index sensor based on parallel-connected dual Fabry-Perot interferometers with Vernier effect. *Sensors Actuators A Phys.* **2019**, *290*, 14–19. [[CrossRef](#)]
15. Flores, R.; Janeiro, R.; Viegas, J. Optical fibre Fabry-Pérot interferometer based on inline microcavities for salinity and temperature sensing. *Sci. Rep.* **2019**, *9*, 9556. [[CrossRef](#)] [[PubMed](#)]
16. Wu, Y.; Liu, B.; Wu, J.; Zhao, L.; Sun, T.; Mao, Y.; Nan, T.; Wang, J. A transverse load sensor with ultra-sensitivity employing Vernier-effect improved parallel-structured fiber-optic Fabry-Perot interferometer. *IEEE Access* **2019**, *7*, 120297–120303. [[CrossRef](#)]
17. Han, Z.; Xin, G.; Nan, P.; Liu, J.; Zhu, J.; Yang, H. Hypersensitive high-temperature gas pressure sensor with Vernier effect by two parallel Fabry-Perot interferometers. *Optik* **2021**, *241*, 166956. [[CrossRef](#)]
18. Hou, L.; Zhao, C.; Xu, B.; Mao, B.; Shen, C.; Wang, D. Highly sensitive PDMS-filled Fabry-Perot interferometer temperature sensor based on the Vernier effect. *Appl. Opt.* **2019**, *58*, 4858–4865. [[CrossRef](#)] [[PubMed](#)]
19. Pan, R.; Yang, W.; Li, L.; Yang, Y.; Zhang, L.; Yu, X.; Fan, J.; Yu, S.; Xiong, Y. A High-Sensitive Fiber-Optic Fabry-Perot Sensor with Parallel Polymer-Air Cavities based on Vernier Effect for Simultaneous Measurement of Pressure and Temperature. *IEEE Sens. J.* **2021**, *21*, 21577–21585. [[CrossRef](#)]
20. Su, H.; Zhang, Y.; Zhao, Y.; Ma, K.; Qi, K.; Guo, Y.; Zhu, F. Parallel double-FPIs temperature sensor based on suspended-core microstructured optical fiber. *IEEE Photonics Technol. Lett.* **2019**, *31*, 1905–1908. [[CrossRef](#)]
21. Liu, J.; Nan, P.; Tian, Q.; Sun, X.; Yang, H.; Yang, H. Sensitivity Enhanced Strain Sensor Based on Two-Arm Vernier Effect. *IEEE Photonics Technol. Lett.* **2021**, *33*, 375–378. [[CrossRef](#)]
22. Zhang, J.; Liao, H.; Lu, P.; Jiang, X.; Fu, X.; Ni, W.; Liu, D.; Zhang, J. Ultrasensitive temperature sensor with cascaded fiber optic Fabry-Perot interferometers based on Vernier effect. *IEEE Photonics J.* **2018**, *10*, 1–11. [[CrossRef](#)]
23. Paixão, T.; Araújo, F.; Antunes, P. Highly sensitive fiber optic temperature and strain sensor based on an intrinsic Fabry-Perot interferometer fabricated by a femtosecond laser. *Opt. Lett.* **2019**, *44*, 4833–4836. [[CrossRef](#)]
24. Paixão, T.; Ferreira, R.; Araújo, F.; Antunes, P. Hybrid intrinsic optical fiber sensor fabricated by femtosecond laser with enhanced sensitivity by Vernier effect. *Opt. Laser Technol.* **2021**, *133*, 106520. [[CrossRef](#)]
25. Zhao, Y.; Jiang, J.; Yang, Y.; Wang, Y.; Lu, J.; Jiacheng, L. High-Sensitive All-Fiber Fabry-Perot Interferometer Gas Refractive Index Sensor Based on Lateral offset Splicing and Vernier Effect. In Proceedings of the 2019 IEEE 18th International Conference on Optical Communications and Networks (ICOON), Huangshan, China, 5–8 August 2019; pp. 1–3.
26. Li, Y.; Zhao, C.; Xu, B.; Wang, D.; Yang, M. Optical cascaded Fabry-Perot interferometer hydrogen sensor based on Vernier effect. *Opt. Commun.* **2018**, *414*, 166–171. [[CrossRef](#)]
27. Li, Z.; Zhang, Y.X.; Zhang, W.G.; Kong, L.X.; Yan, T.Y.; Geng, P.C.; Wang, B. High-sensitivity gas pressure Fabry-Perot fiber probe with micro-channel based on Vernier effect. *J. Light. Technol.* **2019**, *37*, 3444–3451. [[CrossRef](#)]
28. Zhang, P.; Tang, M.; Gao, F.; Zhu, B.; Zhao, Z.; Duan, L.; Fu, S.; Ouyang, J.; Wei, H.; Shum, P.P. Simplified hollow-core fiber-based Fabry-Perot interferometer with modified Vernier effect for highly sensitive high-temperature measurement. *IEEE Photonics J.* **2015**, *7*, 7100210. [[CrossRef](#)]
29. Quan, M.; Tian, J.; Yao, Y. Ultra-high sensitivity Fabry-Perot interferometer gas refractive index fiber sensor based on photonic crystal fiber and Vernier effect. *Opt. Lett.* **2015**, *40*, 4891–4894. [[CrossRef](#)] [[PubMed](#)]
30. Kong, L.; Zhang, Y.; Zhang, W.; Zhang, Y.; Yu, L.; Yan, T.; Geng, P. Cylinder-type fiber-optic Vernier probe based on cascaded Fabry-Perot interferometers with a controlled FSR ratio. *Appl. Opt.* **2018**, *57*, 5043–5047. [[CrossRef](#)] [[PubMed](#)]
31. Chen, P.; Dai, Y.; Zhang, D.; Wen, X.; Yang, M. Cascaded-cavity Fabry-Perot interferometric gas pressure sensor based on Vernier effect. *Sensors* **2018**, *18*, 3677. [[CrossRef](#)] [[PubMed](#)]
32. Wang, F.; Liu, Y.; Lu, Y.; Zhang, L.; Ma, J.; Wang, L.; Sun, W. High-sensitivity Fabry-Perot interferometer temperature sensor probe based on liquid crystal and the Vernier effect. *Opt. Lett.* **2018**, *43*, 5355–5358. [[CrossRef](#)] [[PubMed](#)]
33. Zhang, W.; Liu, Y.; Zhang, T.; Yang, D.; Wang, Y.; Yu, D. Integrated fiber-optic Fabry-Perot interferometer sensor for simultaneous measurement of liquid refractive index and temperature. *IEEE Sens. J.* **2019**, *19*, 5007–5013. [[CrossRef](#)]
34. Zhao, C.; Han, F.; Li, Y.; Mao, B.; Kang, J.; Shen, C.; Dong, X. Volatile Organic Compound Sensor Based on PDMS Coated Fabry-Perot Interferometer with Vernier Effect. *IEEE Sens. J.* **2019**, *19*, 4443–4450. [[CrossRef](#)]
35. Zhang, G.; Wu, X.; Zhang, W.; Li, S.; Shi, J.; Zuo, C.; Fang, S.; Yu, B. High temperature Vernier probe utilizing photonic crystal fiber-based Fabry-Perot interferometers. *Opt. Express* **2019**, *27*, 37308–37317. [[CrossRef](#)]
36. Lang, C.; Liu, Y.; Liao, Y.; Li, J.; Qu, S. Ultra-sensitive fiber-optic temperature sensor consisting of cascaded liquid-air cavities based on Vernier effect. *IEEE Sens. J.* **2020**, *20*, 5286–5291. [[CrossRef](#)]
37. Gomes, A.D.; Becker, M.; Dellith, J.; Zibaii, M.I.; Latifi, H.; Rothhardt, M.; Bartelt, H.; Frazão, O. Multimode Fabry-Perot interferometer probe based on Vernier effect for enhanced temperature sensing. *Sensors* **2019**, *19*, 453. [[CrossRef](#)]
38. Yang, X.; Wu, S.; Cheng, H.; Ma, J.; Wang, S.; Liu, S.; Lu, P. Simplified highly-sensitive gas pressure sensor based on harmonic Vernier effect. *Opt. Laser Technol.* **2021**, *140*, 107007. [[CrossRef](#)]

39. Pan, R.; Yang, W.; Li, L.; Yang, Y.; Yu, X.; Fan, J.; Yu, S.; Xiong, Y.; Zhang, L. All-fiber Fabry-Perot interferometer gas refractive index sensor based on hole-assisted one-core fiber and Vernier effect. *IEEE Sens. J.* **2021**, *21*, 15417–15424. [[CrossRef](#)]
40. Yang, Y.; Zhang, X.; Yang, L.; Yu, Y.; Wang, Z.; Wang, T. Ultrahigh-sensitivity displacement sensing enabled by the Vernier effect with inhibited antiresonance. *Opt. Lett.* **2021**, *46*, 1053–1056. [[CrossRef](#)]
41. Zhou, C.; Zhou, Q.; Wang, B.; Tian, J.; Yao, Y. High-sensitivity relative humidity fiber-optic sensor based on an internal–external Fabry–Perot cavity Vernier effect. *Optics Express* **2021**, *29*, 11854–11868. [[CrossRef](#)]
42. Fu, X.; Ran, R.; Li, Q.; Zhang, R.; Li, D.; Fu, G.; Jin, W.; Bi, W.; Qi, Y.; Hu, Q. A sensitivity-enhanced temperature sensor with end-coated PDMS in few mode fiber based on Vernier effect. *Opt. Commun.* **2021**, *497*, 127173. [[CrossRef](#)]
43. Xie, M.; Gong, H.; Zhang, J.; Zhao, C.L.; Dong, X. Vernier effect of two cascaded in-fiber Mach–Zehnder interferometers based on a spherical-shaped structure. *Appl. Opt.* **2019**, *58*, 6204–6210. [[CrossRef](#)] [[PubMed](#)]
44. Lu, C.; Dong, X.; Lu, L.; Guan, Y.; Ding, S. Label free all-fiber static pressure sensor based on Vernier effect with temperature compensation. *IEEE Sens. J.* **2020**, *20*, 4726–4731. [[CrossRef](#)]
45. Zhao, Y.; Lin, H.; Zhou, C.; Deng, H.; Zhou, A.; Yuan, L. Cascaded Mach–Zehnder interferometers with Vernier effect for gas pressure sensing. *IEEE Photonics Technol. Lett.* **2019**, *31*, 591–594. [[CrossRef](#)]
46. Lin, H.; Liu, F.; Dai, Y.; Zhou, A. Cascaded fiber Mach–Zehnder interferometers for Sensitivity-enhanced gas pressure measurement. *IEEE Sens. J.* **2018**, *19*, 2581–2586. [[CrossRef](#)]
47. Lin, H.; Liu, F.; Guo, H.; Zhou, A.; Dai, Y. Ultra-highly sensitive gas pressure sensor based on dual side-hole fiber interferometers with Vernier effect. *Opt. Express* **2018**, *26*, 28763–28772. [[CrossRef](#)] [[PubMed](#)]
48. Ni, W.; Lu, P.; Fu, X.; Sun, H.; Shum, P.P.; Liao, H.; Jiang, X.; Liu, D.; Yang, C.; Zhang, J. Simultaneous implementation of enhanced resolution and large dynamic range for fiber temperature sensing based on different optical transmission mechanisms. *Opt. Express* **2018**, *26*, 18341–18350. [[CrossRef](#)]
49. Hu, J.; Shao, L.; Gu, G.; Zhang, X.; Liu, Y.; Song, X.; Song, Z.; Feng, J.; Buczyński, R.; Śmietana, M. Dual Mach–Zehnder interferometer based on side-hole fiber for high-sensitivity refractive index sensing. *IEEE Photonics J.* **2019**, *11*, 1–13. [[CrossRef](#)]
50. Wang, Z.; Huang, L.; Liu, C.; Wang, H.; Sun, S.; Yang, D. Sensitivity-Enhanced Fiber Temperature Sensor Based on Vernier Effect and Dual In-Line Mach–Zehnder Interferometers. *IEEE Sens. J.* **2019**, *19*, 7983–7987. [[CrossRef](#)]
51. Li, J.; Cheng, H.; Lin, H.; Li, H.; Zhou, A. Ultrasensitive measurement of gas refractive index based on cascaded Mach–Zehnder interferometers and Vernier effect. *Meas. Sci. Technol.* **2021**, *32*, 095108. [[CrossRef](#)]
52. Xie, L.; Sun, B.; Chen, M.; Zhang, Z. Sensitivity enhanced temperature sensor with serial tapered two-mode fibers based on the Vernier effect. *Opt. Express* **2020**, *28*, 32447–32455. [[CrossRef](#)] [[PubMed](#)]
53. Gu, S.; Feng, D.; Zhang, T.; Deng, S.; Li, M.; Hu, Y.; Sun, W.; Deng, M. Highly Sensitive Magnetic Field Measurement With Taper-Based In-Line Mach-Zehnder Interferometer and Vernier Effect. *J. Light. Technol.* **2022**, *40*, 909–917. [[CrossRef](#)]
54. Guillen-Ruiz, L.; Anzueto-Sánchez, G.; Torres-Gómez, I.; Camas-Anzueto, J.; Martínez-Rios, A.; Salceda-Delgado, G. Experimental demonstration of optical Vernier effect by cascading tapered single-mode optical fibres. *Opt. Fiber Technol.* **2022**, *70*, 102869. [[CrossRef](#)]
55. Zhang, S.; Liu, Y.; Guo, H.; Zhou, A.; Yuan, L. Highly sensitive vector curvature sensor based on two juxtaposed fiber Michelson interferometers with Vernier-like effect. *IEEE Sens. J.* **2018**, *19*, 2148–2154. [[CrossRef](#)]
56. Zhang, S.; Yin, L.; Zhao, Y.; Zhou, A.; Yuan, L. Bending sensor with parallel fiber Michelson interferometers based on Vernier-like effect. *Opt. Laser Technol.* **2019**, *120*, 105679. [[CrossRef](#)]
57. Li, Z.; Zhang, Y.X.; Zhang, W.G.; Kong, L.X.; Yue, Y.; Yan, T.Y. Parallelized fiber Michelson interferometers with advanced curvature sensitivity plus abated temperature crosstalk. *Opt. Lett.* **2020**, *45*, 4996–4999. [[CrossRef](#)] [[PubMed](#)]
58. Shao, L.Y.; Luo, Y.; Zhang, Z.; Zou, X.; Luo, B.; Pan, W.; Yan, L. Sensitivity-enhanced temperature sensor with cascaded fiber optic Sagnac interferometers based on Vernier-effect. *Opt. Commun.* **2015**, *336*, 73–76. [[CrossRef](#)]
59. Liu, Q.; Xing, L.; Wu, Z.; Fu, Y.; Li, S.; Xue, P.; Ng, W.P.; Wu, Q.; Binns, R. Cascaded Sagnac Loops Embedded With Two Polarization Maintaining Photonic Crystal Fibers for Highly Sensitive Strain Measurement. *IEEE Trans. Instrum. Meas.* **2021**, *70*, 7002309. [[CrossRef](#)]
60. Robalinho, P.M.R.; Gomes, A.D.; Frazao, O. High enhancement strain sensor based on Vernier effect using 2-Fiber loop mirrors. *IEEE Photonics Technol. Lett.* **2020**, *32*, 1139–1142. [[CrossRef](#)]
61. Liu, S.; Lu, G.; Lv, D.; Chen, M.; Zhang, Z. Sensitivity enhanced temperature sensor with cascaded Sagnac loops based on harmonic Vernier effect. *Opt. Fiber Technol.* **2021**, *66*, 102654. [[CrossRef](#)]
62. Shao, L.Y.; Zhang, X.; He, H.; Zhang, Z.; Zou, X.; Luo, B.; Pan, W.; Yan, L. Optical fiber temperature and torsion sensor based on Lyot-Sagnac interferometer. *Sensors* **2016**, *16*, 1774. [[CrossRef](#)] [[PubMed](#)]
63. Wu, B.; Zhao, C.; Xu, B.; Li, Y. Optical fiber hydrogen sensor with single Sagnac interferometer loop based on Vernier effect. *Sens. Actuators B Chem.* **2018**, *255*, 3011–3016. [[CrossRef](#)]
64. Liu, S.; Lu, P.; Chen, E.; Ni, W.; Liu, D.; Zhang, J.; Lian, Z. Vernier effect of fiber interferometer based on cascaded PANDA polarization maintaining fiber. *Chin. Opt. Lett.* **2019**, *17*, 080601. [[CrossRef](#)]
65. Wu, B.; Chen, L.; Zhao, C.; Chan, C.C. Polypyrrole-coated polarization maintaining fiber-based Vernier effect for isopropanol measurement. *J. Light. Technol.* **2019**, *37*, 2768–2772. [[CrossRef](#)]
66. Li, K.; Zhang, N.; Zhang, N.M.Y.; Zhou, W.; Zhang, T.; Chen, M.; Wei, L. Birefringence induced Vernier effect in optical fiber modal interferometers for enhanced sensing. *Sens. Actuators B Chem.* **2018**, *275*, 16–24. [[CrossRef](#)]

67. Chen, G.T.; Zhang, Y.X.; Zhang, W.G.; Kong, L.X.; Zhao, X.; Zhang, Y.; Li, Z.; Yan, T.Y. Double helix microfiber coupler enhances refractive index sensing based on Vernier effect. *Opt. Fiber Technol.* **2020**, *54*, 102112. [[CrossRef](#)]
68. Jiang, Y.; Yi, Y.; Brambilla, G.; Wang, P. Ultra-high-sensitivity refractive index sensor based on dual-microfiber coupler structure with the Vernier effect. *Opt. Lett.* **2020**, *45*, 1268–1271. [[CrossRef](#)]
69. Jiang, Y.; Yi, Y.; Brambilla, G.; Wang, P. High-sensitivity, fast-response ethanol gas optical sensor based on a dual microfiber coupler structure with the Vernier effect. *Opt. Lett.* **2021**, *46*, 1558–1561. [[CrossRef](#)] [[PubMed](#)]
70. Zamora, V.; Lützow, P.; Weiland, M.; Pergande, D. A highly sensitive refractometric sensor based on cascaded SiN microring resonators. *Sensors* **2013**, *13*, 14601–14610. [[CrossRef](#)] [[PubMed](#)]
71. Xu, Z.; Sun, Q.; Li, B.; Luo, Y.; Lu, W.; Liu, D.; Shum, P.P.; Zhang, L. Highly sensitive refractive index sensor based on cascaded microfiber knots with Vernier effect. *Opt. Express* **2015**, *23*, 6662–6672. [[CrossRef](#)] [[PubMed](#)]
72. Ying, Y.; Zhao, C.; Gong, H.; Shang, S.; Hou, L. Demodulation method of Fabry-Perot sensor by cascading a traditional Mach-Zehnder interferometer. *Opt. Laser Technol.* **2019**, *118*, 126–131. [[CrossRef](#)]
73. Li, J.; Zhang, M.; Wan, M.; Lin, C.; Huang, S.; Liu, C.; He, Q.; Qiu, X.; Fang, X. Ultrasensitive refractive index sensor based on enhanced Vernier effect through cascaded fiber core-offset pairs. *Opt. Express* **2020**, *28*, 4145–4155. [[CrossRef](#)] [[PubMed](#)]
74. Yang, Y.; Wang, Y.; Zhao, Y.; Jiang, J.; He, X.; Yang, W.; Zhu, Z.; Gao, W.; Li, L. Sensitivity-enhanced temperature sensor by hybrid cascaded configuration of a Sagnac loop and a FP cavity. *Opt. Express* **2017**, *25*, 33290–33296. [[CrossRef](#)]
75. Wang, S.; Wang, S.; Jin, R.B.; Feng, M.; Wu, S.; Zhang, L.; Lu, P. All-optical demodulation fiber acoustic sensor with real-time controllable sensitivity based on optical Vernier effect. *IEEE Photonics J.* **2019**, *11*, 6801911. [[CrossRef](#)]
76. Liu, L.; Ning, T.; Zheng, J.; Pei, L.; Li, J.; Cao, J.; Gao, X.; Zhang, C. High-sensitivity strain sensor implemented by hybrid cascaded interferometers and the Vernier-effect. *Opt. Laser Technol.* **2019**, *119*, 105591. [[CrossRef](#)]
77. Jia, X.; Zhou, X.; Bi, M.; Yang, G.; Hu, M.; Wang, T. High-sensitivity optical fiber temperature sensor of cascaded FSI and MZI based on Vernier effect. *Opt. Fiber Technol.* **2021**, *65*, 102625. [[CrossRef](#)]
78. Xu, Z.; Luo, Y.; Liu, D.; Shum, P.P.; Sun, Q. Sensitivity-controllable refractive index sensor based on reflective θ -shaped microfiber resonator cooperated with Vernier effect. *Sci. Rep.* **2017**, *7*, 9620. [[CrossRef](#)] [[PubMed](#)]
79. Cai, L.; Xia, F.; Zhang, H.x.; Zhao, Y. Temperature Sensing Characteristics of an MKR in a Microfiber Taper Based on Mechanisms of Interference and Resonance with Vernier Effect. *Opt. Lasers Eng.* **2021**, *143*, 106617. [[CrossRef](#)]
80. Abbas, L.G.; Li, H. Temperature sensing by hybrid interferometer based on Vernier like effect. *Opt. Fiber Technol.* **2021**, *64*, 102538. [[CrossRef](#)]
81. Gomes, A.D.; Ferreira, M.S.; Bierlich, J.; Kobelke, J.; Rothhardt, M.; Bartelt, H.; Frazao, O. Hollow microsphere combined with optical harmonic Vernier effect for strain and temperature discrimination. *Opt. Laser Technol.* **2020**, *127*, 106198. [[CrossRef](#)]